

MATERIALS SCIENCE

Strained hybrid perovskite thin films and their impact on the intrinsic stability of perovskite solar cells

Jingjing Zhao,¹ Yehao Deng,¹ Haotong Wei,¹ Xiaopeng Zheng,¹ Zhenhua Yu,¹ Yuchuan Shao,¹ Jeffrey E. Shield,¹ Jinsong Huang^{1,2*}

Organic-inorganic hybrid perovskite (OIHP) solar cells have achieved comparable efficiencies to those of commercial solar cells, although their instability hinders their commercialization. Although encapsulation techniques have been developed to protect OIHP solar cells from external stimuli such as moisture, oxygen, and ultraviolet light, understanding of the origin of the intrinsic instability of perovskite films is needed to improve their stability. We show that the OIHP films fabricated by existing methods are strained and that strain is caused by mismatched thermal expansion of perovskite films and substrates during the thermal annealing process. The polycrystalline films have compressive strain in the out-of-plane direction and in-plane tensile strain. The strain accelerates degradation of perovskite films under illumination, which can be explained by increased ion migration in strained OIHP films. This study points out an avenue to enhance the intrinsic stability of perovskite films and solar cells by reducing residual strain in perovskite films.

INTRODUCTION

Organic-inorganic hybrid perovskites (OIHPs) are regarded as one of the most promising candidates for solar cells due to their extraordinary optoelectronic properties for photon-to-electron conversion, as well as their solution processability (1–3), large light absorption coefficient (4), long diffusion length (5–9), and large carrier mobility (10). In the past few years, the power conversion efficiency (PCE) of OIHP solar cells with a size of a few square millimeters has increased to more than 22% (11), and the PCE of larger-area ($>1\text{-cm}^2$) OIHP pixel devices has exceeded 20% (12). However, instability problems remain as the largest challenge for commercialization of OIHP solar cells (13). OIHPs are reported to be sensitive to many external stimuli, such as moisture (14–16), oxygen (17), and ultraviolet light (18–20). The corrosion of charge transport layers (21) or common metal electrodes by OIHPs (22, 23) represents another important channel of cell failure. To enhance device stability, encapsulation techniques are being developed to protect OIHP solar cells from the ambient environment (24–26), and alternative corrosion-resistant metal electrodes (27–31), corrosion-blocking layers (32–34) that separate OIHP films from metal electrodes, and charge transport layers have been explored. On the other hand, there are far fewer studies on the intrinsic instability mechanism in OIHP films, although the intrinsic instability may dominate device degradation once the degradation caused by external stimuli is solved for OIHP solar cells. Once the degradation of the perovskite devices by external stimuli is suppressed, the intrinsic stability of perovskite films will impose the limitation on the stability of perovskite solar cells. Jacobsson *et al.* (35) reported a large thermal expansion coefficient of methylammonium lead iodide perovskites and raised the concern of thermally induced instability of perovskite solar cells during day/night operation. However, it is not yet clear how the large thermal expansion coefficient affects not only the quality of perovskite films but also the intrinsic stability of perovskite films.

Here, we report the observation of lattice strain in OIHP films fabricated by existing methods involving thermal annealing and the study of its impact on the intrinsic stability of OIHP solar cells. The

origin of lattice strain and the mechanism of strain-induced instability are revealed. We anticipate that the successful identification and solving of strain-induced degradation represent a direction to improve the intrinsic stability of OIHP solar cells.

RESULTS

Strain in perovskite polycrystalline thin films

The presence of lattice strain in regular perovskite films for high-efficiency solar cells was revealed by comparing the spin-coated $\text{CH}_3\text{NH}_3\text{PbI}_3$ (MAPbI₃) on poly(triarylamine) (PTAA)-covered indium tin oxide (ITO)/glass substrates to the loose MAPbI₃ powder. The spun MAPbI₃ films were prepared by the antisolvent method, as described in Materials and Methods. Briefly, toluene was used as antisolvent during spin-coating of the MAPbI₃ precursor solution. The MAPbI₃ films were formed by annealing at 100°C for 10 min. The freestanding MAPbI₃ powder was prepared by scraping the as-prepared perovskite films from the substrates. The out-of-plane x-ray diffraction (XRD) spectra of the MAPbI₃ film and MAPbI₃ powder are shown in Fig. 1A. The MAPbI₃ film on the ITO/glass substrate showed XRD peaks at $2\theta = 14.02^\circ$, 40.58° , and 43.13° , corresponding to (110), (224), and (314) planes, respectively. For the powder sample, all the peaks showed up but shifted to lower diffraction angles. The (110) peak shifted by 0.07° , and the (224) and (314) peaks shifted by 0.15° . The shift of XRD peaks for higher index planes is larger, which is a signature for the presence of lattice strain in either the film and/or the powder sample. Note that the sample position has been carefully aligned before measuring the thin-film and powder sample, so the peak shift is not caused by film thickness variation.

To determine which sample(s) was (were) strained, freestanding perovskites with approximately millimeter-sized single crystals were synthesized as the strain-free control samples. The XRD peak positions of the single-crystal powder matched well with those of the powder but not the films, indicating that the films on the substrates are strained. The out-of-plane XRD measures the spacing of crystal planes perpendicular to the substrate, as illustrated in Fig. 1C. A shift of a diffraction peak to higher diffraction angles, as observed in the films, corresponds to smaller plane spacing, and thus, the strain is compressive in the normal direction of the films. We performed the in-plane XRD, which measures the spacing of the planes in parallel to the substrate, as illustrated in

Copyright © 2017
The Authors, some
rights reserved;
exclusive licensee
American Association
for the Advancement
of Science. No claim to
original U.S. Government
Works. Distributed
under a Creative
Commons Attribution
NonCommercial
License 4.0 (CC BY-NC).

¹Department of Mechanical and Materials Engineering and Nebraska Center for Materials and Nanoscience, University of Nebraska-Lincoln, Lincoln, NE 68588, USA. ²Department of Applied Physical Sciences, University of North Carolina, Chapel Hill, NC 27599, USA.

*Corresponding author. Email: jhuang@unc.edu

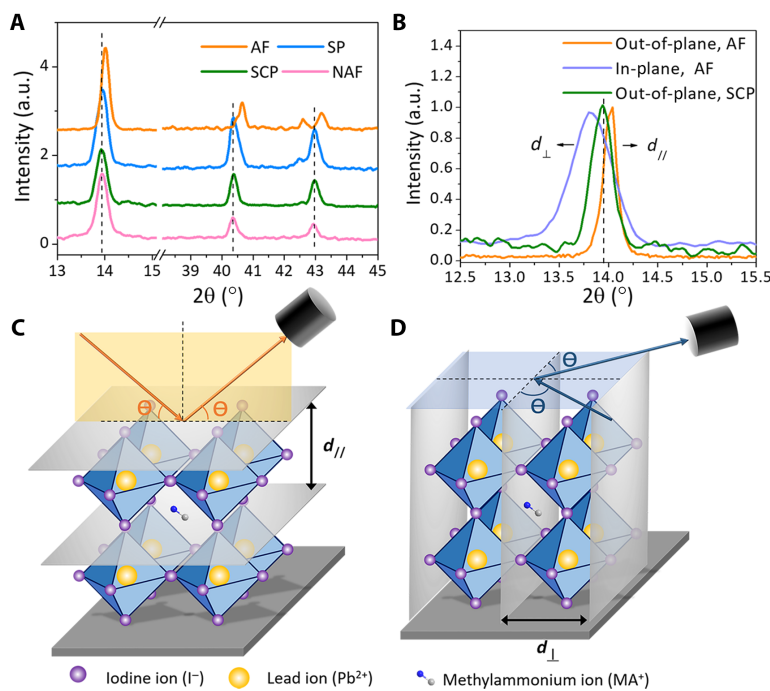


Fig. 1. Characterization of strain. (A) Out-of-plane XRD of the MAPbI₃ annealed film (AF), scraped powder (SP), single-crystal powder (SCP), and non-annealed film (NAF). a.u., arbitrary unit. (B) In-plane and out-of-plane XRD of AF and out-of-plane XRD of SCP. (C and D) Schematic architecture of the out-of-plane (C) and in-plane (D) XRD.

Fig. 1D. The result of the (110) diffraction peak is shown in Fig. 1B, together with the out-of-plane peak. It can be observed that the (110) in-plane peak shifted to a lower angle as compared to the strain-free peak of the single crystals, indicating a tensile strain in the horizontal direction for the polycrystalline MAPbI₃ film.

We also examined whether lattice strain exists in OIHP films prepared by other methods, including one-step spin-coating (36, 37), two-step spin-coating (1, 38), and doctor blade-coating (28). As shown in fig. S1A, all the MAPbI₃ films on ITO substrates had the (110) peak at $2\theta = 14.02^\circ$. When the films fabricated by different methods were scraped from the substrates, the peaks shifted to lower angles, which match those of the nonstrained perovskite single crystals. Further, perovskite films with different compositions, including formamidine (FA)-containing perovskite [FA_{0.85}MA_{0.15}Pb(I_{0.85}Br_{0.15})₃] and cesium (Cs)-containing perovskite [Cs_{0.05}(FA_{0.85}MA_{0.15})_{0.95}Pb(I_{0.85}Br_{0.15})₃], which have been used to make high-efficiency (~21%) solar cells (39, 40), have also been investigated. As shown in fig. S1 (C and D), when the films were scraped from the substrates, the XRD peaks also shifted to lower angles. The fact that scraping OIHP powder from the substrates releases the lattice strain indicates that the substrates have strong adhesion to OIHP at room temperature, which maintains the lattice strain in the OIHP layer. The substrate on which OIHP is strained is not limited to PTAA/ITO/glass, because OIHP on other substrates generally used for high-efficiency solar cells, such as SnO₂-covered ITO glass, Al₂O₃-covered ITO glass, or TiO₂-covered FTO (fluorine-doped tin oxide) glass, also displayed peak shifts relative to the single-crystal OIHP (fig. S1B). Therefore, lattice strain generally exists in OIHP films, which are used for high-efficiency perovskite solar cells.

Origin of the lattice strain

The fact that perovskite films prepared by different methods had similar lattice strain indicates that the strain should originate from a shared pro-

cess that all these OIHP films have experienced. The film formation process is largely different in the three film deposition methods. In one-step spin-coating with antisolvent, the perovskite film is formed by a phase transformation from an MAPbI₃-DMSO (dimethyl sulfoxide) intermediate phase (41). In two-step spin-coating, it is formed by a solid-solid reaction between spin-coated PbI₂ and methylammonium iodide (MAI) stacking layers (42). In blade coating, the film directly crystallizes from the precursor solution without going through the intermediate phase (43). However, all the films were formed at temperatures of $\geq 100^\circ\text{C}$, whereas the strain measurements were performed at room temperature. We conducted the XRD measurement of the MAPbI₃ thin films on ITO substrates at 100°C and found that the films were not strained. We then recorded the XRD peak evolution during cooling from 100°C to room temperature and found that the strain gradually appeared in the thin-film sample. Because thermal expansion of the lattice could account for the peak shift, the peak shift of the scraped MAPbI₃ powder was measured over the same temperature range. However, its peak shift is much smaller than that of the thin film (Fig. 2, C and D), indicating that the peak shift observed in the thin-film materials are mainly due to the introduction of strain. The thermal expansion coefficient of MAPbI₃ was calculated on the basis of the peak shift of the scraped MAPbI₃ powder, as shown in fig. S2. For MAPbI₃ in the tetragonal phase, the average linear expansion coefficient $[(2a + c)/3]$ is $6.1 \times 10^{-5} \text{ K}^{-1}$, which is more than an order of magnitude larger than that of the ITO or glass substrate ($\alpha_{\text{ITO}} = 0.85 \times 10^{-5} \text{ K}^{-1}$ and $\alpha_{\text{glass}} = 0.37 \times 10^{-5} \text{ K}^{-1}$) (44) and close to what Jacobsson *et al.* (35) reported for MAPbI₃ thin-film samples on glass.

Considering the large thermal expansion mismatch between the perovskite and the ITO/glass substrate, we propose strain formation during cooling (Fig. 2, A and B). When the perovskite forming at 100°C cools to room temperature, it tends to contract due to the positive thermal expansion coefficient (Fig. 2A). If a perovskite film is deposited

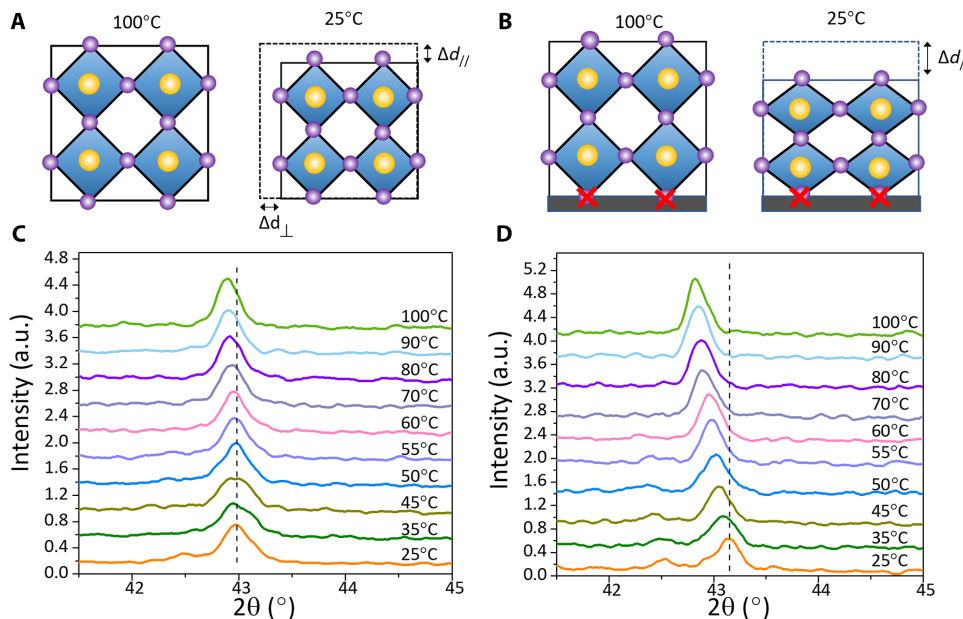


Fig. 2. Schematic diagram and XRD of the strain formation process. (A) Without substrate, the perovskite forming at 100°C contracts vertically and laterally during cooling. (B) With the substrate adhesion, the annealed perovskite film only contracts vertically. (C and D) In situ out-of-plane XRD of scraped powder (C) and annealed film (D) at different temperatures.

on a substrate with a much smaller thermal expansion coefficient, then the perovskite in contact with the substrate cannot contract, resulting in tensile strain along the in-plane direction. To compensate for the reduced lateral shrinkage upon cooling, the film shrinks more in the out-of-plane direction, resulting in compressive strain in this direction. To verify this, we used a flexible substrate of polyethylene terephthalate (PET) with a thermal expansion coefficient of $\alpha = 2 \times 10^{-5}$ to $8 \times 10^{-5} \text{ K}^{-1}$, close to that of MAPbI_3 . As shown in fig. S3, the lattice strain in the MAPbI_3 film on the PET substrate is much smaller than that on the ITO/glass substrate.

The amount of lattice strain should be critically determined by the temperature at which the perovskite is formed. We also prepared MAPbI_3 films at room temperature by drying the as-spun MAPbI_3 -DMSO intermediate phase by evacuating for 3 days instead of annealing at 100°C (45). It was found that the XRD peaks of the MAPbI_3 film formed at room temperature were coincident with the peaks of the nonstrained crystals, as shown by the pink line in Fig. 1A, further confirming our hypothesis. Note that MAPbI_3 film experiences a phase transformation when it is cooled from 100°C to room temperature. However, the phase transformation should not be the origin of strain, because mixed-cations/halides perovskite films, which do not have a phase transformation in this temperature range, are still strained. In addition, we prepared MAPbI_3 films by annealing at temperatures slightly below or above the phase transformation temperature and found that the two kinds of films have similar degrees of strain by XRD (fig. S4). It further eliminates phase transformation as the origin of strain. On the other hand, the residual lattice strain was found to be insensitive to post-annealing history, that is, regular thermal annealing after film formation cannot completely release the lattice strain. As shown in fig. S5, the nonstrained MAPbI_3 film is still unstrained after being annealed at 100°C for 4 hours, whereas the strained film was still strained even after being annealed at 100°C for 20 hours. Again, this is due to the strong adhesion of perovskite to the substrate once the perovskite is formed.

Therefore, the strain is difficult to completely eliminate in the perovskite films once formed during high-temperature processing. Although regular thermal annealing can induce grain growth and coarsening, which can reduce grain boundary defect density and improve carrier transport properties, it cannot release the strain of the perovskite films grown on substrates.

Impact of strain on film stability

Strain engineering has been broadly applied in the semiconductor industry to achieve fast transistors with both compressive and tensile strain. Although it is not yet clear how the strain affects the electronic properties of the OIHPs, a strong impact of the lattice strain on their stability in these polycrystalline films was reported here. To observe the impact of strain on film stability under illumination, we tuned the strain in the perovskite films by preparing MAPbI_3 films on thin glass substrates, which are bendable. A thin layer ($\sim 40 \text{ nm}$) of polystyrene (PS) was coated on top of the MAPbI_3 layers to cover the perovskites and prevent the surface decomposition initiated by moisture. Then, the films were bent in a convex shape to increase the lattice strain or in a concave shape to reduce the residual strain in the films, which is illustrated in the inset of Fig. 3. The changing of the lattice strain of the bent films was verified by out-of-plane XRD spectra, as shown in fig. S6. The lattice strain in the convex, flat, and concave films were approximately 0.2, 0.47, and 0.62%, respectively.

Three samples with different bending states were sealed together in a petri dish and illuminated by white light with an intensity of $\sim 50 \text{ mW/cm}^2$, and the geometry of the measurement is shown in Fig. 3A. The temperature of the samples was not intentionally controlled but was measured to be around 65°C during the stability study. After illumination for 500 hours, the bending force was removed, and the films were set back to the flat state for measurements. The photographic images in Fig. 3A show that the films with larger lattice strain had large areas that turned yellow, which is generally a signature of the

decomposition of MAPbI_3 into PbI_2 , whereas the films with the smallest strain remained mostly black after 500-hour illumination. The XRD pattern shown in Fig. 3B confirmed the results. It is noticed that there is regional difference in the degree of degradation within one film. It is not caused by different degrees of strain at different locations because we confirmed that the strain is uniform over the film (fig. S7). This difference can be caused by different grain sizes, defect concentrations, etc. at different locations as a result of the spin-coating process. The intensity ratio of the (001) PbI_2 peak to the (110) MAPbI_3 peak is 1.09 for the convex film with the largest strain and 0.43 for the flat film with the intermediate strain. The concave film with the smallest strain was stable after illumination for 500 hours without any appearance of the PbI_2 peak.

Another interesting observation is that if the strain is released before decomposition occurs, then the perovskite film is more stable. Here, we etched ITO to expose glass on one-half of an ITO/glass substrate, and MAPbI_3 films were deposited on the same substrates to ensure the same film quality on both ITO and glass. The scanning electron microscopy image of MAPbI_3 films on the two types of substrates is shown in fig. S8. The grain size and distribution were virtually identical on the two substrates. Therefore, the previously observed influence of grain size on perovskite film stability does not affect this study (46). MAPbI_3 films coated on PTAA/ITO and PTAA/glass surfaces were measured by XRD every 7 days under continuous illumination, and the spectra are shown in Fig. 4 (A and B). Because glass is much smoother than ITO, it is expected to allow easier strain relaxation because of less affinity or bonding of perovskite to the very smooth and nonwetting glass substrate, whereas the hydrophobic PTAA further enhances the separation of MAPbI_3 from glass. The MAPbI_3 film still has certain affinity to the PTAA-covered ITO substrate, because the roughness of ITO is comparable or larger than the PTAA thickness (10 nm). Initially, the XRD peak positions of the films on ITO and glass are the same, indicating the same degree of strain in MAPbI_3 on the two different surfaces. The strain relaxation process was studied by XRD peak shift, and the degree of MAPbI_3 decomposition was defined by the XRD peak intensity ratio between the (001) PbI_2 peak and the (110) MAPbI_3 peak. The results are summarized in Fig. 4 (C and D). The strain relaxation was accelerated by exposing the uncovered MAPbI₃ films to illumination. Under continuous illumination, the XRD peaks of the MAPbI_3 film

on glass gradually shifted to lower angles, indicating that the strain was largely relaxed in 7 days. After strain relaxation, the MAPbI_3 film on glass was stable for 3 weeks without the appearance of any PbI_2 XRD peaks. On the other hand, the strain of the MAPbI_3 film on ITO was not relaxed in the first 2 weeks, as indicated by the lack of shift in the XRD peaks. The decomposition of the MAPbI_3 film was observed in this period with an increasing (001) PbI_2 /(110) MAPbI_3 XRD peak ratio. The strain partially relaxed after 3 weeks, because the XRD peaks of the film on ITO shifted slightly to lower angles, and the rate of film decomposition decreased.

Besides the PTAA/ITO/glass substrate, SnO_2 /ITO/glass has been tested to observe the relation between strain and stability of the perovskite films, and the results are shown in fig. S9. We found that for all substrates, the strain effects on the stability of perovskite films was consistently the same, that is, the degradation is accelerated if the strain is present in the MAPbI_3 films; if the strain is relaxed, then the MAPbI_3 films are more stable.

Mechanism of accelerated degradation by strain

Because the decomposition of solid-state MAPbI_3 to PbI_2 involves mass transport, the accelerated degradation by strain should be related to the change of ion migration under strain. Thus, the activation energy (E_a) for ion migration in the MAPbI_3 films was measured in the dark and under illumination. The samples were prepared on the flexible substrates by the one-step deposition process, followed by the thermal evaporation of Au bar electrodes with a spacing of 50 μm . A layer of PS was then coated on top of the MAPbI_3 films. Then, the films were bent to different strain states to enhance or reduce the lattice strain, which is also illustrated in the insets of Fig. 5. The temperature-dependent conductivity was measured by the following previously established processes (47, 48), and the results are shown in Fig. 5. On the basis of the Nernst-Einstein relationship

$$\sigma T = \sigma_0 \exp(-E_a/kT) \quad (1)$$

where σ_0 and k are constants, σ and T are conductivity and temperature, respectively, and E_a is the activation energy for ion migration. E_a can be derived from the slope of the $\ln(\sigma T)$ versus $1/T$ plot. As shown

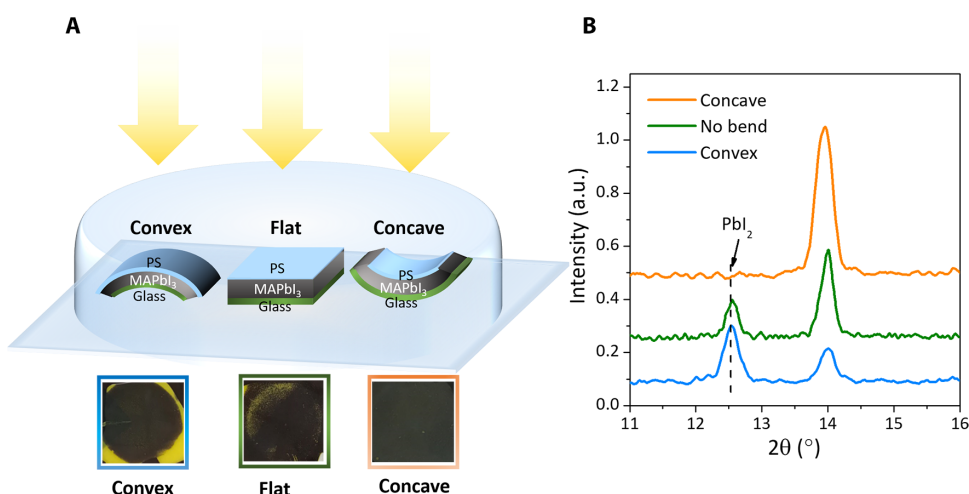


Fig. 3. Strain impact on perovskite film stability. (A) Schematic diagram of the experimental setup of the films with different strains and photographs of the films with different strains after 500-hour illumination. (B) Out-of-plane XRD of the three films in (A).

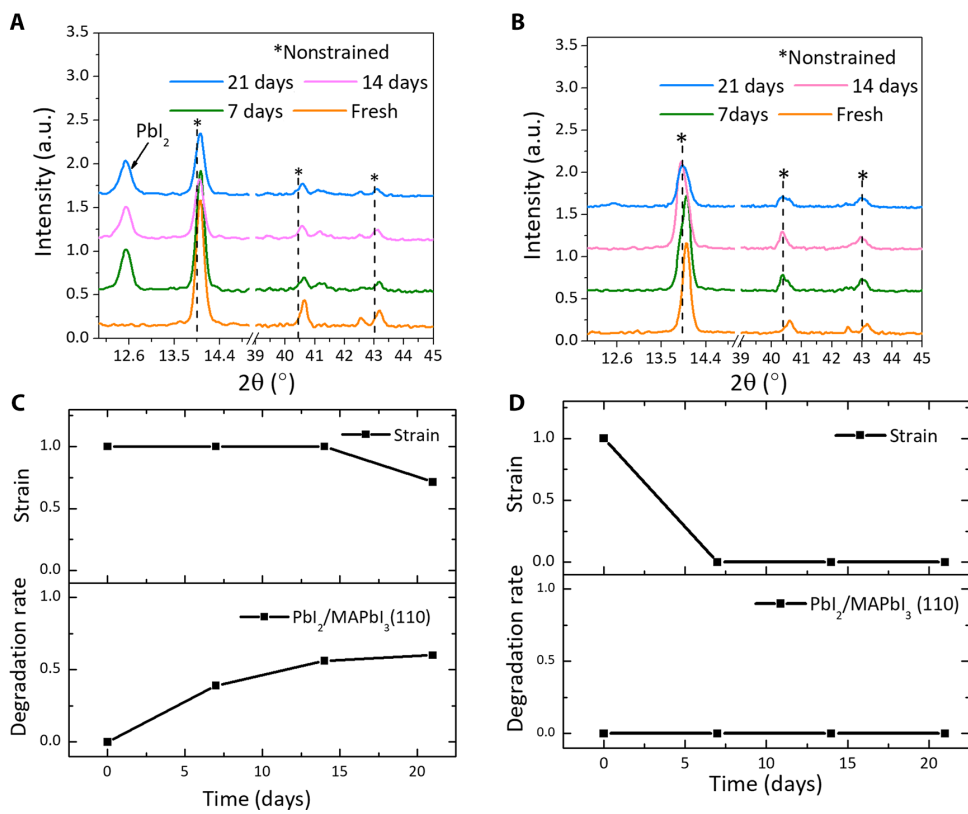


Fig. 4. Strain and degradation of MAPbI_3 film on the ITO/glass substrate. (A and B) Out-of-plane XRD of the annealed film on the ITO side (A) and glass side (B) as a function of illumination time. (C and D) Strain and degradation rate of the annealed film on the ITO side (C) and glass side (D) as a function of time concluded from (A) and (B).

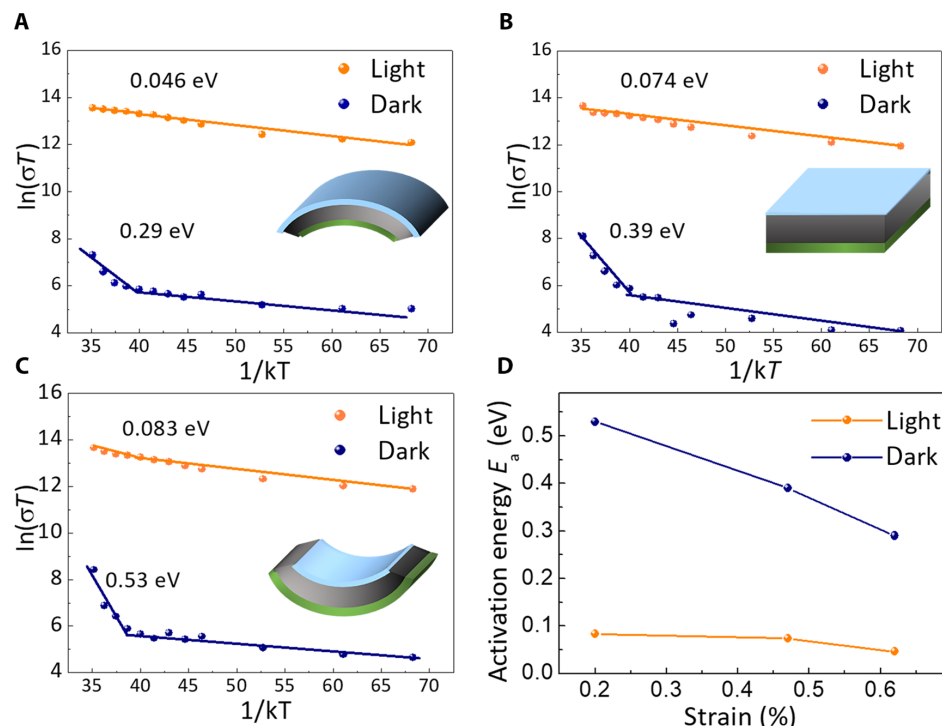


Fig. 5. Ion migration properties of MAPbI_3 films with different strains. (A to C) The temperature-dependent conductivity of the convex film (A), the flat film (B), and the concave film (C). Inset: Schematic diagram of the samples. (D) Variation of the activation energy of ion migration versus the strain in the MAPbI_3 films.

in Fig. 5, the activation energies for ion migration are 0.29, 0.39, and 0.53 eV for the convex, flat, and concave MAPbI_3 films, respectively. Under illumination by white light with an intensity of 25 mW/cm², the activation energies for ion migration reduced to 0.046, 0.074, and 0.083 eV for the convex, flat, and concave films, respectively. The result conclusively shows that the perovskite films with larger strain have smaller ion migration activation energy in both dark or under illumination conditions. The accelerated ion migration in the strained perovskite films can explain the faster degradation of MAPbI_3 into PbI_2 , because MA^+ and I^- ions can migrate more easily from the MAPbI_3 films, producing PbI_2 . The increased ion migration under larger lattice strain can be explained by the additional driving force caused by the strain for ion migration, because the ion migration process relaxes the lattice strain and thus reduces the free energy of the system.

DISCUSSION

In conclusion, we discovered that lattice strain is present in perovskite films formed by high-temperature annealing processes used for the fabrication of all high-efficiency perovskite solar cells. The strain is caused by the thermal expansion mismatch between the perovskite material and substrate. The lattice strain is found to be an important intrinsic source of instability in perovskite films reducing the activation energy for ion migration, which then accelerates perovskite decomposition. Relaxation of the lattice strain or avoiding the generation of the lattice strain can decrease the strain-related perovskite decomposition rate. We found that low-temperature perovskite film formation or using substrates with a similar thermal expansion coefficient can minimize fabrication-induced strain, providing a path to enhance intrinsic perovskite device stability, and should be taken into account in the design of scalable fabrication of perovskite solar modules. Finally, the strain-related film stability is not limited to solar cells and may influence the stability of other electronic materials.

MATERIALS AND METHODS

Perovskite thin-film fabrication

MAPbI_3 perovskite films made by the one-step method were prepared from a precursor solution (1.3 M) of equal molar ratio of PbI_2 and MAI in a mixed solvent of 9:1 volume ratio of dimethylformamide (DMF) and DMSO in a N_2 -filled glove box. After the ITO/glass or cover glass substrates were cleaned by isopropanol, acetone, and treated by ultraviolet-ozone plasma, PTAA/toluene solution (2 mg/ml) was spin-coated on the ITO/glass substrates at 4000 rpm for 30 s. After the PTAA-coated ITO/glass substrates were annealed at 100°C for 10 min, the perovskite precursor solution was spin-coated on top of the substrates at 4000 rpm for 20 s. One hundred thirty microliters of toluene was dripped on the substrate after the substrate was spinning for 10 s. Then, the coated substrates were either annealed at 100°C for 10 min or transferred to a vacuum chamber for 3 days, as previously reported to fabricate the annealed and the non-annealed samples, respectively.

MAPbI_3 perovskite films made by doctor blading were prepared from a precursor solution (1 M) of equal molar ratio of PbI_2 and MAI in DMF. After the substrates were treated as above, they were set on a hot plate at a temperature of 145°C. Then, the precursor solution was dropped and swiped by an applicator with a speed of 1 cm/s. After the film was formed, it was annealed at 100°C for 10 min.

MAPbI_3 perovskite films made by the two-step method were prepared by a PbI_2 /DMF solution (650 mg/ml) and MAI/IPA solution (65 mg/ml). After the substrate was prepared as above, 35 μl of the pre-heated PbI_2 precursor solution was spin-coated on top of it at a speed of 6000 rpm. After the PbI_2 -coated substrate was annealed at 100°C for 10 min, 55 μl of the MAI precursor solution was spin-coated on top of it at 6000 rpm. Then, the prepared films were annealed at 100°C for 30 min.

Perovskite single-crystal powder preparation

$\text{Pb}(\text{Ac})_2 \cdot 3\text{H}_2\text{O}$ (2.5 g; 99%, Alfa Aesar) was dissolved into 7.6 ml of aqueous HI solution (57% w/w, stabilized with 1.5% hypophosphorus acid; Alfa Aesar) under stirring at 110°C, and 6.6 mM aqueous methylamine solution (CH_3NH_2) (40% w/w; Alfa Aesar) was dissolved into 0.87 ml of HI under stirring for 10 min. The methylamine mixture solution was then gradually dropped into the $\text{Pb}(\text{Ac})_2 \cdot 3\text{H}_2\text{O}$ mixture solution under stirring at 110°C, and a black MAPbI_3 powder was obtained at the bottom of the solution. The solution was kept stirring at 80°C for 1 hour, and then, the black powder was separated from the solution and washed for at least three times with diethyl ether. The MAPbI_3 powder was then dried under vacuum overnight.

Stability test

All the samples were stored in one petri dish and sealed by a plastic bag in air with ~30% relative humidity and illuminated under white light with an intensity of 50 mW/cm².

Activation energy determination

To characterize the activation energy for ion migration, lateral devices were fabricated by thermal depositing Au electrodes with a spacing of 50 μm on top of the annealed films. A thin layer (40 nm) of PS was spin-coated on top of the device. Then, the devices were bent to different states and set in a Lakeshore Probe Station under a vacuum of 10⁻⁵ Pa with 0.25-sun white light through a quartz window. The samples with different bending states were settled on a copper plate where the temperature was controlled by a heater and liquid N_2 . The electric field of the lateral device was 1.2 V/ μm . The current was measured by a Keithley 2400 at different temperatures. The device was first cooled and stabilized at 170 K for 30 min. Then, the device was slowly heated to 330 K with a step of 10 K. Each step was stabilized at that temperature for 10 min before the current measurement was taken.

Characterization of perovskites by XRD

Out-of-plane XRD measurements were performed with a Bruker AXS D8 Discover diffractometer. Bruker D8 Discover diffractometer was configured in parallel beam geometry with $\text{Cu K}\alpha$ radiation (a wavelength of 1.5418 Å). The in situ XRD at different temperatures was measured by this diffractometer with a domed hot stage. In-plane XRD measurements were carried out with the Rigaku SmartLab diffractometer using $\text{Cu K}\alpha$ radiation (a wavelength of 1.5418 Å).

Lattice calculation

The lattice parameters were determined using standard extrapolation techniques (49). Both a and c were obtained by the extrapolation of the lattice constant versus $\cos^2(\theta)/\sin(\theta)$, which provided a better fit to the data than did $\cos^2(\theta)$ extrapolation from different peaks. Peak positions were determined by fitting the XRD peaks with a Gaussian function.

SUPPLEMENTARY MATERIALS

Supplementary material for this article is available at <http://advances.sciencemag.org/cgi/content/full/3/11/eaao5616/DC1>

- fig. S1. Strain state of MAPbI_3 films and scraped powder made by different methods on different substrates and with different compositions.
- fig. S2. In situ out-of-plane XRD and the calculated lattice parameter of the MAPbI_3 powder under different temperatures.
- fig. S3. Strain state for MAPbI_3 on PET substrate.
- fig. S4. Strain state of MAPbI_3 films formed at different temperatures.
- fig. S5. Effect of post-annealing on strain state.
- fig. S6. Out-of-plane XRD of the MAPbI_3 on a flexible substrate with different bending states.
- fig. S7. Distribution of strain on the substrate.
- fig. S8. Morphology of MAPbI_3 film on PTAA/ITO and PTAA/glass substrates.
- fig. S9. Degradation of strained MAPbI_3 film on SnO_2 substrate under illumination.

REFERENCES AND NOTES

1. J. Burschka, N. Pellet, S.-J. Moon, R. Humphry-Baker, P. Gao, M. K. Nazeeruddin, M. Grätzel, Sequential deposition as a route to high-performance perovskite-sensitized solar cells. *Nature* **499**, 316–319 (2013).
2. D. Liu, T. L. Kelly, Perovskite solar cells with a planar heterojunction structure prepared using room-temperature solution processing techniques. *Nat. Photonics* **8**, 133–138 (2014).
3. M. Yang, Z. Li, M. O. Reese, O. G. Reid, D. H. Kim, S. Siol, T. R. Klein, Y. Yan, J. J. Berry, M. F. A. M. van Hest, K. Zhu, Perovskite ink with wide processing window for scalable high-efficiency solar cells. *Nat. Energy* **2**, 17038 (2017).
4. M. A. Green, A. Ho-Baillie, H. J. Snaith, The emergence of perovskite solar cells. *Nat. Photonics* **8**, 506–514 (2014).
5. S. D. Stranks, G. E. Eperon, G. Grancini, C. Menelaou, M. J. P. Alcocer, T. Leijtens, L. M. Herz, A. Petrozza, H. J. Snaith, Electron-hole diffusion lengths exceeding 1 micrometer in an organometal trihalide perovskite absorber. *Science* **342**, 341–344 (2013).
6. Q. Dong, Y. Fang, Y. Shao, P. Mulligan, J. Qiu, L. Cao, J. Huang, Electron-hole diffusion lengths > 175 μm in solution-grown $\text{CH}_3\text{NH}_3\text{PbI}_3$ single crystals. *Science* **347**, 967–970 (2015).
7. M. D. McGehee, Perovskite solar cells: Continuing to soar. *Nat. Mater.* **13**, 845–846 (2014).
8. D. Zhao, Y. Yu, C. Wang, W. Liao, N. Shrestha, C. R. Grice, A. J. Cimaroni, L. Guan, R. J. Ellingson, K. Zhu, X. Zhao, R.-G. Xiong, Y. Yan, Low-bandgap mixed tin-lead iodide perovskite absorbers with long carrier lifetimes for all-perovskite tandem solar cells. *Nat. Energy* **2**, 17018 (2017).
9. D. Shi, V. Adinolfi, R. Comin, M. Yuan, E. Alarousu, A. Buin, Y. Chen, S. Hoogland, A. Rothenberger, K. Katsiev, Y. Losoviy, X. Zhang, P. A. Dowben, O. F. Mohammed, E. H. Sargent, O. M. Bakr, Low trap-state density and long carrier diffusion in organolead trihalide perovskite single crystals. *Science* **347**, 519–522 (2015).
10. C. Wehrenfennig, G. E. Eperon, M. B. Johnston, H. J. Snaith, L. M. Herz, High charge carrier mobilities and lifetimes in organolead trihalide perovskites. *Adv. Mater.* **26**, 1584–1589 (2014).
11. W. S. Yang, B.-W. Park, E. H. Jung, N. J. Jeon, Y. C. Kim, D. U. Lee, S. S. Shin, J. Seo, E. K. Kim, J. H. Noh, S. I. Seok, Iodide management in formamidinium-lead-halide-based perovskite layers for efficient solar cells. *Science* **356**, 1376–1379 (2017).
12. X. Li, D. Bi, C. Yi, J.-D. Décuppet, J. Luo, S. M. Zakeeruddin, A. Hagfeldt, M. Grätzel, A vacuum flash-assisted solution process for high-efficiency large-area perovskite solar cells. *Science* **353**, 58–62 (2016).
13. T. Leijtens, G. E. Eperon, N. K. Noel, S. N. Habermeier, A. Petrozza, H. J. Snaith, Stability of metal halide perovskite solar cells. *Adv. Energy Mater.* **5**, 1500963 (2015).
14. J. Yang, B. D. Siemelkamp, D. Liu, T. L. Kelly, Investigation of $\text{CH}_3\text{NH}_3\text{PbI}_3$ degradation rates and mechanisms in controlled humidity environments using in situ techniques. *ACS Nano* **9**, 1955–1963 (2015).
15. S. Yang, Y. Wang, P. Liu, Y.-B. Cheng, H. J. Zhao, H. G. Yang, Functionalization of perovskite thin films with moisture-tolerant molecules. *Nat. Energy* **1**, 15016 (2016).
16. J. A. Christians, P. A. Miranda Herrera, P. V. Kamat, Transformation of the excited state and photovoltaic efficiency of $\text{CH}_3\text{NH}_3\text{PbI}_3$ perovskite upon controlled exposure to humidified air. *J. Am. Chem. Soc.* **137**, 1530–1538 (2015).
17. N. Aristidou, C. Eames, I. Sanchez-Molina, X. Bu, J. Kosco, M. S. Islam, S. A. Haque, Fast oxygen diffusion and iodide defects mediate oxygen-induced degradation of perovskite solar cells. *Nat. Commun.* **8**, 15218 (2017).
18. D. Bryant, N. Aristidou, S. Pont, I. Sanchez-Molina, T. Chotchunangatchaval, S. Wheeler, J. R. Durrant, S. A. Haque, Light and oxygen induced degradation limits the operational stability of methylammonium lead triiodide perovskite solar cells. *Energy Environ. Sci.* **9**, 1655–1660 (2016).
19. T. Leijtens, G. E. Eperon, S. Pathak, A. Abate, M. M. Lee, H. J. Snaith, Overcoming ultraviolet light instability of sensitized TiO_2 with meso-superstructured organometal tri-halide perovskite solar cells. *Nat. Commun.* **4**, 2885 (2013).
20. S. Wang, Y. Jiang, E. J. Juarez-Perez, L. K. Ono, Y. Qi, Accelerated degradation of methylammonium lead iodide perovskites induced by exposure to iodine vapour. *Nat. Energy* **2**, 16195 (2016).
21. W. R. Mateker, M. D. McGehee, Progress in understanding degradation mechanisms and improving stability in organic photovoltaics. *Adv. Mater.* **29**, 1603940 (2017).
22. Y. Han, S. Meyer, Y. Okhissi, K. Weber, J. M. Pringle, U. Bach, L. Spiccia, Y.-B. Cheng, Degradation observations of encapsulated planar $\text{CH}_3\text{NH}_3\text{PbI}_3$ perovskite solar cells at high temperatures and humidity. *J. Mater. Chem. A* **3**, 8139–8147 (2015).
23. Y. Kato, L. K. Ono, M. V. Lee, S. Wang, S. R. Raga, Y. Qi, Silver iodide formation in methyl ammonium lead iodide perovskite solar cells with silver top electrodes. *Adv. Mater. Interfaces* **2**, 1500195 (2015).
24. J.-W. Lee, D.-H. Kim, H.-S. Kim, S.-W. Seo, S. M. Cho, N.-G. Park, Formamidinium and cesium hybridization for photo- and moisture-stable perovskite solar cell. *Adv. Energy Mater.* **5**, 1501310 (2015).
25. K. A. Bush, A. F. Palmstrom, Z. J. Yu, M. Boccard, R. Cheacharoen, J. P. Mailoa, D. P. McMeekin, R. L. Z. Hoye, C. D. Baille, T. Leijtens, I. M. Peters, M. C. Minichetti, N. Rolston, R. Prasanna, S. Sofia, D. Harwood, W. Ma, F. Moghadam, H. J. Snaith, T. Buonassis, Z. C. Holman, S. F. Bent, M. D. McGehee, 23.6%-efficient monolithic perovskite/silicon tandem solar cells with improved stability. *Nat. Energy* **2**, 17009 (2017).
26. X. Li, M. Tschumi, H. Han, S. B. Babkair, R. A. Alzubaydi, A. A. Ansari, S. S. Habib, M. K. Nazeeruddin, S. M. Zakeeruddin, M. Grätzel, Outdoor performance and stability under elevated temperatures and long-term light soaking of triple-layer mesoporous perovskite photovoltaics. *Energy Technol.* **3**, 551–555 (2015).
27. J. Zhao, X. Zheng, Y. Deng, T. Li, Y. Shao, A. Gruber, J. Shield, J. Huang, Is Cu a stable electrode material in hybrid perovskite solar cells for a 30-year lifetime? *Energy Environ. Sci.* **9**, 3650–3656 (2016).
28. Y. Deng, Q. Dong, C. Bi, Y. Yuan, J. Huang, Air-stable, efficient mixed-cation perovskite solar cells with Cu electrode by scalable fabrication of active layer. *Adv. Energy Mater.* **6**, 1600372 (2016).
29. A. Mei, X. Li, L. Liu, Z. Ku, T. Liu, Y. Rong, M. Xu, M. Hu, J. Chen, Y. Yang, M. Grätzel, H. Han, A hole-conductor-free, fully printable mesoscopic perovskite solar cell with high stability. *Science* **345**, 295–298 (2014).
30. M. Kaltenbrunner, G. Adam, E. D. Glowacki, M. Drack, R. Schwödauer, L. Leonat, D. H. Apaydin, H. Groiss, M. C. Scharber, M. S. White, N. S. Sariciftci, S. Bauer, Flexible high power-per-weight perovskite solar cells with chromium oxide–metal contacts for improved stability in air. *Nat. Mater.* **14**, 1032–1039 (2015).
31. K. A. Bush, C. D. Baille, Y. Chen, A. R. Bowring, W. Wang, W. Ma, T. Leijtens, F. Moghadam, M. D. McGehee, Thermal and environmental stability of semi-transparent perovskite solar cells for tandems enabled by a solution-processed nanoparticle buffer layer and sputtered ITO electrode. *Adv. Mater.* **28**, 3937–3943 (2016).
32. X. Dong, X. Fang, M. Lv, B. Lin, S. Zhang, J. Ding, N. Yuan, Improvement of the humidity stability of organic–inorganic perovskite solar cells using ultrathin Al_2O_3 layers prepared by atomic layer deposition. *J. Mater. Chem. A* **3**, 5360–5367 (2015).
33. J. You, L. Meng, T.-B. Song, T.-F. Guo, Y. Yang, W.-H. Chang, Z. Hong, H. Chen, H. Zhou, Q. Chen, Y. Liu, N. De Marco, Y. Yang, Improved air stability of perovskite solar cells via solution-processed metal oxide transport layers. *Nat. Nanotechnol.* **11**, 75–81 (2016).
34. W. Chen, Y. Wu, Y. Yue, J. Liu, W. Zhang, X. Yang, H. Chen, E. Bi, I. Ashraful, M. Grätzel, L. Han, Efficient and stable large-area perovskite solar cells with inorganic charge extraction layers. *Science* **350**, 944–948 (2015).
35. T. J. Jacobsson, L. J. Schwan, M. Ottosson, A. Hagfeldt, T. Edvinsson, Determination of thermal expansion coefficients and locating the temperature-induced phase transition in methylammonium lead perovskites using x-ray diffraction. *Inorg. Chem.* **54**, 10678–10685 (2015).
36. J. H. Heo, S. H. Im, J. H. Noh, T. N. Mandal, C.-S. Lim, J. A. Chang, Y. H. Lee, H.-j. Kim, A. Sarkar, Md. K. Nazeeruddin, M. Grätzel, S. I. Seok, Efficient inorganic–organic hybrid heterojunction solar cells containing perovskite compound and polymeric hole conductors. *Nat. Photonics* **7**, 486–491 (2013).
37. M. M. Lee, J. Teuscher, T. Miyasaka, T. N. Murakami, H. J. Snaith, Efficient hybrid solar cells based on meso-superstructured organometal halide perovskites. *Science* **338**, 643–647 (2012).
38. Z. Xiao, C. Bi, Y. Shao, Q. Dong, Q. Wang, Y. Yuan, C. Wang, Y. Gao, J. Huang, Efficient, high yield perovskite photovoltaic devices grown by interdiffusion of solution-processed precursor stacking layers. *Energy Environ. Sci.* **7**, 2619–2623 (2014).
39. M. Saliba, T. Matsui, J.-Y. Seo, K. Domanski, J.-P. Correa-Baena, M. K. Nazeeruddin, S. M. Zakeeruddin, W. Tress, A. Abate, A. Hagfeldt, M. Grätzel, Cesium-containing triple cation perovskite solar cells: Improved stability, reproducibility and high efficiency. *Energy Environ. Sci.* **9**, 1989–1997 (2016).
40. X. Zheng, B. Chen, J. Dai, Y. Fang, Y. Bai, Y. Lin, H. Wei, X. C. Zeng, J. Huang, Defect passivation in hybrid perovskite solar cells using quaternary ammonium halide anions and cations. *Nat. Energy* **2**, 17102 (2017).
41. T. M. Brenner, Y. Rakita, Y. Orr, E. Klein, I. Feldman, M. Elbaum, D. Cahen, G. Hodes, Conversion of single crystalline PbI_2 to $\text{CH}_3\text{NH}_3\text{PbI}_3$: Structural relations and transformation dynamics. *Chem. Mater.* **28**, 6501–6510 (2016).

42. S. Yang, Y. C. Zheng, Y. Hou, X. Chen, Y. Chen, Y. Wang, H. Zhao, H. G. Yang, Formation mechanism of freestanding $\text{CH}_3\text{NH}_3\text{PbI}_3$ functional crystals: In situ transformation vs dissolution-crystallization. *Chem. Mater.* **26**, 6705–6710 (2014).
43. Q. Hu, L. Zhao, J. Wu, K. Gao, D. Luo, Y. Jiang, Z. Zhang, C. Zhu, E. Schaible, A. Hexemer, C. Wang, Y. Liu, W. Zhang, M. Grätzel, F. Liu, T. P. Russell, R. Zhu, Q. Gong, In situ dynamic observations of perovskite crystallisation and microstructure evolution intermediated from $[\text{PbI}_6]^{4-}$ cage nanoparticles. *Nat. Commun.* **8**, 15688 (2017).
44. V. Craciun, D. Craciun, X. Wang, T. J. Anderson, R. K. Singh, Transparent and conducting indium tin oxide thin films grown by pulsed laser deposition at low temperatures. *J. Optoelectron. Adv. Mater.* **5**, 401–408 (2003).
45. G. Xing, N. Mathews, S. S. Lim, N. Yantara, X. Liu, D. Sabba, M. Grätzel, S. Mhaisalkar, T. C. Sum, Low-temperature solution-processed wavelength-tunable perovskites for lasing. *Nat. Mater.* **13**, 476–480 (2014).
46. Q. Wang, B. Chen, Y. Liu, Y. Deng, Y. Bai, Q. Dong, J. Huang, Scaling behavior of moisture-induced grain degradation in polycrystalline hybrid perovskite thin films. *Energy Environ. Sci.* **10**, 516–522 (2017).
47. J. Xing, Q. Wang, Q. Dong, Y. Yuan, Y. Fang, J. Huang, Ultrafast ion migration in hybrid perovskite polycrystalline thin films under light and suppression in single crystals. *Phys. Chem. Chem. Phys.* **18**, 30484–30490 (2016).
48. Y. Yuan, J. Chae, Y. Shao, Q. Wang, Z. Xiao, A. Centrone, J. Huang, Photovoltaic switching mechanism in lateral structure hybrid perovskite solar cells. *Adv. Energy Mater.* **5**, 1500615 (2015).
49. B. D. Cullity, S. R. Stock, *Elements of X-Ray Diffraction* (Prentice-Hall, ed. 3, 2001).

Acknowledgments

Funding: This work was supported by Office of Naval Research (grant numbers N00014-15-1-2713 and N00014-17-1-2163). The research was performed in part in the Nebraska Nanoscale Facility: National Nanotechnology Coordinated Infrastructure, the Nebraska Center for Materials and Nanoscience, and the Nanoengineering Research Core Facility, which are supported by the NSF (Award ECCS 1542182), and the Nebraska Research Initiative. **Author contributions:** J.H. conceived the idea. J.H., J.Z., and J.E.S. designed the experiments. J.Z. and Y.D. conducted the characterization. Y.D. fabricated the doctor blading films. H.W. synthesized the single-crystal powder. X.Z. and Z.Y. fabricated the mixed-cation perovskite films. J.Z. and Y.S. did the experiment of the film degradation on the ITO/glass substrate. J.H. and J.Z. wrote the paper. All authors reviewed the paper. **Competing interests:** The authors declare that they have no competing interests. **Data and materials availability:** All data needed to evaluate the conclusions in the paper are present in the paper and/or the Supplementary Materials. Additional data related to this paper may be requested from the authors.

Submitted 4 August 2017

Accepted 23 October 2017

Published 17 November 2017

10.1126/sciadv.aa05616

Citation: J. Zhao, Y. Deng, H. Wei, X. Zheng, Z. Yu, Y. Shao, J. E. Shield, J. Huang, Strained hybrid perovskite thin films and their impact on the intrinsic stability of perovskite solar cells. *Sci. Adv.* **3**, eaao5616 (2017).